RESEARCH ARTICLE

ADVANCED OPTICAL MATERIALS
www.advopticalmat.de

Accurate Optical Metrology of van der Waals Monolayers and Heterostructures from the Interference of Interface Polariton Waves

*Kang Qin, Zong-yan Zuo, Sheng Peng, Kai Liu, Hui Yang, Qi-hang Zhang, Yan-qing Lu, Yong-yuan Zhu, and Xue-jin Zhang**

New two-dimensional (2D) van der Waals materials are emerging, and their optical parameters urgently need to be acquired experimentally. Most of the reported results come from traditional metrologies used in the past for bulk materials. This unavoidably causes controversy regarding the correctness and accuracy of results, as well as the physical model. Surface/interface plasmon polariton waves are sub-diffraction-limited and very sensitive to surroundings. Here, 2D van der Waals materials with metal embodied are presented. Surface/interface exciton-plasmon polaritons come into being with excitons in 2D transition-metal dichalcogenides (TMDCs), which are physically taken as the boundary conditions with complex optical conductivities at the interfaces. Complex optical conductivities of 2D TMDCs are measured by means of interference behavior of surface/interface polariton waves. The size requirement of 2D van der Waals materials becomes relaxed, and complex optical conductivities can be measured for single-crystalline WS_2 and MoS_2 monolayers with small sizes. Furthermore, a remarkable capability is manifested by yielding complex optical conductivity of van der Waals heterostructures. The proposed metrology can apply to other newly developed materials with modified underlying physical models, as well as various types of 2D van der Waals materials.

1. Introduction

Two-dimensional (2D) materials have attracted considerable interest since the isolation of single-layer graphite, namely graphene, in 2004.[1] The atomic thickness gives them natural advantages in nanophotonics. The tunable Fermi energy of graphene makes it of great application value in adjustable devices,[2,3] such as optical modulators,[4] tunable sensors,[5,6] and infrared photodetectors.[7] As a matter of fact, graphene's zero band gap limits its application in nanoscale light sources. In recent years, a kind of thin transition-metal dichalcogenides (TMDCs) came into view. Mo- and W-based dichalcogenides have thickness-dependent optical properties.[8-10] In particular, they exhibit indirect-to-direct band gap semiconductors when the thickness is reduced to monolayer.[9] The recombination of electron-hole pairs inside TMDCs can emit visible or near-infrared light.[11-15] Furthermore, with interlayer interaction within vertical heterostructures, a new type of exciton, i.e., interlayer exciton can be formed.[12,13] The interlayer exciton energy is determined by the energy level of the original elements. Hence emission wavelengths can be extended by combining different kinds of elemental materials.[11,13]

As the central parameter, optical parameters of 2D materials is susceptible to the preparation process and surroundings, such as temperature and number of layers.[16-18] The measurements of optical parameters become particularly important and have been carried out predominantly using spectroscopic ellipsometry (SE).[18-21] With the lower limit of actual spot size, typically 300 μm in diameter,[22] this traditional measurement method inevitably has minimum size requirements for the sample. To be more practical, much effort has been put into the pursuit of high spatial resolution, by integrating SE into optical microscopy or vice versa.[23,24] Differential reflectance spectroscopy (DRS) can be considered as the derivative of SE,[17,25] such as optical absorption and transient transmission/reflection techniques.[26] DRS enables measurements with a spatial resolution of sub-10 μm using microscopy. However, for both SE and DRS methods, the accuracy of measurements based on the Fresnel Equation is determined by the collimation and polarization of incident light. In common systems with dispersive optical elements, it is usually

---

K. Qin, Z.-yan Zuo, S. Peng, K. Liu, H. Yang, Q.-hang Zhang, Y.-qing Lu, Y.-yuan Zhu, X.-jin Zhang
National Laboratory of Solid State Microstructures
and Collaborative Innovation Center of Advanced Microstructures
Nanjing University
Nanjing 210093, P. R. China
E-mail: xuejinzh@nju.edu.cn

K. Qin, Q.-hang Zhang, Y.-qing Lu, X.-jin Zhang
Key Laboratory of Intelligent Optical Sensing and Manipulation
and Jiangsu Key Laboratory of Artificial Functional Materials
College of Engineering and Applied Sciences
Nanjing University
Nanjing 210093, P. R. China

Z.-yan Zuo
School of Electronic Science and Engineering
Nanjing University
Nanjing 210093, P. R. China

S. Peng, K. Liu, Y.-yuan Zhu
School of Physics
Nanjing University
Nanjing 210093, P. R. China

The ORCID identification number(s) for the author(s) of this article can be found under https://doi.org/10.1002/adom.202301229

DOI: 10.1002/adom.202301229

necessary to measure one wavelength one time to ensure the accuracy. In a word, the current far-field measurement schemes, e.g. SE and DRS are restricted by the optical diffraction limit and requirements on optical setup, thus normally cannot achieve high spatial resolution.

In recent years, the near-field measurement scheme based on scattering-type scanning near-field optical microscopy (*s*-SNOM) has been developed to collect material information with sub-10 nm spatial resolution, mainly including two types. One is the two-beam interference method, using Fourier transform to obtain an effective index and propagation length.[27] The propagation length is determined by the full width at half maximum of the Fourier spectrum, which is greatly affected by the spatially mapped range of near-field measurements. Generally speaking, the accuracy could be guaranteed only if the measured range reaches the magnitude of the propagation length, which is usually over 100 μm. The other is the optical contrast method, fitting the material parameters to the amplitude and phase collected directly from the near-field signal.[28] However, the shorter the working wavelengths, the larger the background noise scattered by the AFM tip shank and the more difficult the *s*-SNOM phase modulation, leading to a lower accuracy for visible or near-infrared light compared to infrared light. Furthermore, the single-wavelength measurements with low speed of *s*-SNOM would cost much time for the need of continuous spectra measurements.

Taking a completely different approach, we develop a technique based on the multi-beam interference characteristics of surface/interface polariton waves to precisely acquire the complex optical conductivity of 2D materials. This method is immune to the angle of incidence and polarization, reduces the size of 2D materials, and can be widely applicable to the acquisition of optical parameters for various types of 2D materials, no matter whether they are conductive or semiconductive. We treat 2D materials as thicknessless layers at the interfaces of multilayer planar structures, which support guided modes. In consequence, 2D materials enter in the physical model of the guided wave dispersion relation through the boundary conditions when solving Maxwell's equations. In this case, the quantity we need to process is the optical conductivity, which can be transformed to refractive index or dielectric function when wanted as definitive thickness, even though discrepancy and inequivalence have been noted.[29,30]

Here, optical conductivities of single-crystalline WS_2 and MoS_2 monolayers grown by chemical vapor deposition (CVD) and their heterostructures were measured in this way. In order to yield the optical properties of TMDCs at visible or near-infrared wavelength, we construct air/2D TMDC/metal structure, in which surface/interface polariton can be generated. To ensure apparent interference features, single-crystalline Ag is chosen as the metal that can support surface plasmon polariton (SPP) mode,[31,32] based on which the scattering loss of SPP mode can be largely suppressed. Obviously, the complex refractive index or dielectric function of Ag should be first experimentally determined with the excitation of SPP mode propagating at the air/Ag interface. When a TMDC monolayer (heterostructure) is laid on the Ag surface, it constitutes an air/TMDC monolayer (heterostructure)/Ag structure. Assuming isotropic media, the dispersion relation of transverse magnetic surface wave mode can be derived as[33]

$$\frac{\varepsilon_d}{k_d} + \frac{\varepsilon_m}{k_m} = \frac{\sigma_{2D}}{i\omega\varepsilon_0} \tag{1}$$

where ε_d and ε_m are the dielectric functions of media (air and Ag) that sandwich the 2D material (TMDC monolayer or heterostructure), $k_x = k_r + ik_i$ is the wavenumber of surface/interface polariton, and $k_j^2 = k_x^2 - \epsilon_j\omega^2/c^2$ with j = {d, m}. It is noted that the existence of surface/interface polariton waves imposes that the signs of ε_d and ε_m are opposite regardless of whether σ_{2D} is zero or not. If k_r and k_i can be measured, the optical conductivity of 2D TMDC monolayer or heterostructure will be given experimentally from Equation (1).

2. Results and Discussions

As evanescent wave fields, surface/interface polaritons are usually excited by a prism or grating with momentum matching between far-field and near-field light waves. Instead, we experimentally engraved a groove to satisfy the momentum-matching condition. Although it is not as efficient as a prism or grating, one groove is capable of broadband far- and near- field conversion. At the same time, a pair of grooves can launch the interference of surface/interface polariton waves, as a Fabry-Pérot cavity. **Figure 1**a shows the measuring scheme in our experiments. Two parallel grooves were fabricated by focused ion beam etching (Helios 600, FEI Company, 30 keV Ga ions) on the single-crystalline Ag, which are defined as the input and output ends of Fabry–Pérot cavity respectively. The incident white light was focused on the groove of the input end by an objective lens (100×, NA = 0.9). When the incident light hits the groove with two edges, it can be partially coupled into surface/interface polaritons. The guided waves propagate along the surface/interface, and are reflected back and forth between the input and output ends, resulting in the Fabry-Pérot interference phenomenon. A pinhole was placed on the image plane in the detection optical path to collect the signal emitted from the output end and filter out the signal directly scattered by the input one. In the interference spectrum, the light intensity takes a maximum value when $2k_rD = 2q\pi$, and a minimum value when $2k_rD = (2q+1)\pi$, where q stands for non-negative integers and D the distances of two grooves. Therefore, the real part of effective k_r can be extracted from interference fringes.

The imaginary part of effective k_i can be obtained from the oscillation character of interference spectra for several groove pairs with different distances.[34] At a given wavelength, we acquire the minimum intensity (I_{min}) and oscillation strength indicated by the intensity difference (ΔI) between the maximum intensity (I_{max}) and I_{min}, as shown in Figure 1b, then get k_i by fitting the relation curve of $\Delta I/I_{min}$ and groove distances using the following equation[34]

$$\frac{\Delta I}{I_{min}} = \frac{4RA}{(1 - RA)^2} \tag{2}$$

where R is the reflectivity of surface/interface polariton wave at the ends of Fabry–Pérot cavity, and $A = e^{-D/L}$ ($L = 1/(2k_i)$ is the propagation length of surface/interface polariton wave) represents the propagation loss of surface/interface polariton wave.

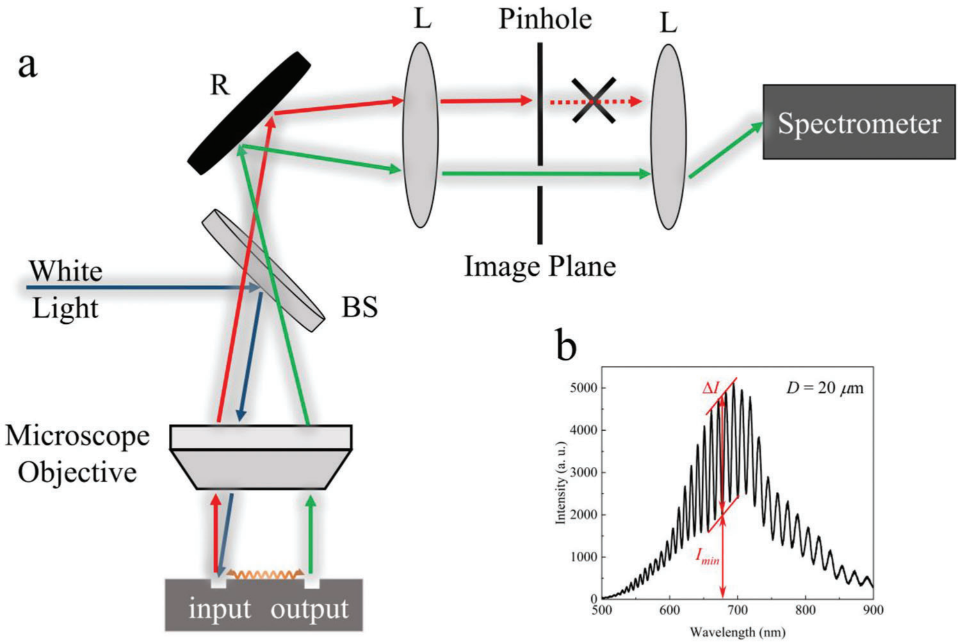

Figure 1. Optical setup and interference fringes. a) Schematic of optical measurement system. R: reflector, BS: beamsplitter, L: lens. b) Interference fringe collected at the output end. D is 20 μm here. The indicator of oscillation ΔI and minimum intensity I_{min} are denoted.

Single-crystalline Ag demonstrates a clear advantage over others, e.g. Ag film prepared from coating, by virtue of atomically flat surface and supporting surface/interface polaritons with quite long propagation length (Figure S1, Supporting Information). The distance D determines the spacing and intensity of interference. Large D comes with a small interference spacing, leading to a more accurate k_r, but lower oscillation strength, which brings difficulty to gain k_i. As a trade-off, we experimentally etched groove pairs with distances equal to 25, 30, 35, and 40 µm (Figure S2, Supporting Information).

In our experiments, single-crystalline WS_2 and MoS_2 monolayers were grown using CVD method and stacked vertically to build heterostructures (Figure S3, Supporting Information).[35] With the help of Raman spectra, WS_2 and MoS_2 monolayer and multilayer can be distinguished (Figure S4, Supporting Information).[36–38] The WS_2/MoS_2 vertical heterostructures were formed by stacking WS_2 and MoS_2 monolayers onto a SiO_2/Si substrate. The side length of heterostructure area is on the order of 50 µm, as shown in Figure 5e. Then the 2D materials were transferred onto single-crystalline Ag with etched groove pairs on surface for interference measurements by the dry transfer method.

The band gaps of WS_2 and MoS_2 are 2.29 and 2.36 eV, respectively. The top valence band of WS_2 is ≈0.35 eV higher than that of MoS_2.[39,40] **Figure 2**a illustrates the energy levels of WS_2/MoS_2 heterostructure with type-II band alignment, in which a new bandgap of ≈2.01 eV is created. The exciton binding energies of WS_2 and MoS_2 are ≈0.29 and 0.5 eV,[41] while that of interlayer excitons is only ≈0.05 eV. The photoluminescence (PL) peaks corresponding to A excitons of WS_2 and MoS_2 will be ≈620 and 670 nm, respectively. After the stacking process, the heterostructures were treated by annealing in a tube furnace under normal pressure at a temperature of 200 °C and a period of 12 h. This step is favorable to guarantee high-quality heterostructures with an effective interlayer interaction by getting rid of water and oxygen molecules, which are easily introduced during transfer process.[12] PL measurements are convenient to identify the emergence of well-defined interlayer transitions. Figure 2b shows PL spectra of the CVD-grown WS_2, MoS_2 monolayers, and their heterostructure. In the visible range, WS_2 monolayer has one obvious peak (≈620 nm) corresponding to A exciton, while MoS_2 monolayer has two peaks (≈670 and ≈625 nm) corresponding to A exciton and B exciton. The PL spectra of the unannealed heterostructure is the direct superposition of the PL spectra of WS_2 and MoS_2, from which the peaks of WS_2 and MoS_2 can be seen. The PL peak intensity of MoS_2 is low compared to that of WS_2. When the interlayer interaction is strong enough, the individual PL peaks of WS_2 and MoS_2 monolayers will disappear and only an interlayer exciton peak (≈630 nm) will be displayed.

The interlayer transition not only leads to the emergence of new exciton level, but also has an effect on the Raman peak position. WS_2 and MoS_2 have two main Raman peaks, A_{1g} and E^1_{2g}, corresponding to first-order out-of-plane and in-plane modes respectively.[36–38] The Raman spectra of WS_2, MoS_2, and their heterostructure are shown in Figure 2c,d. Before annealing, the interlayer interaction is weak, the Raman peak of heterostructure is a direct superposition of the Raman peak of the elemental materials. In contrast, when the interlayer interaction is strong, the Raman peak will shift a little. After annealing, A_{1g} has a blue shift and E^1_{2g} has a red shift.[36,38] Furthermore, both the excitons in MoS_2, WS_2 monolayers and interlayer exciton in WS_2/MoS_2 heterostructure are close related to the surroundings. For instance, the substrate would slightly affect the PL and Raman spectra of them (Figure S5, Supporting Information).

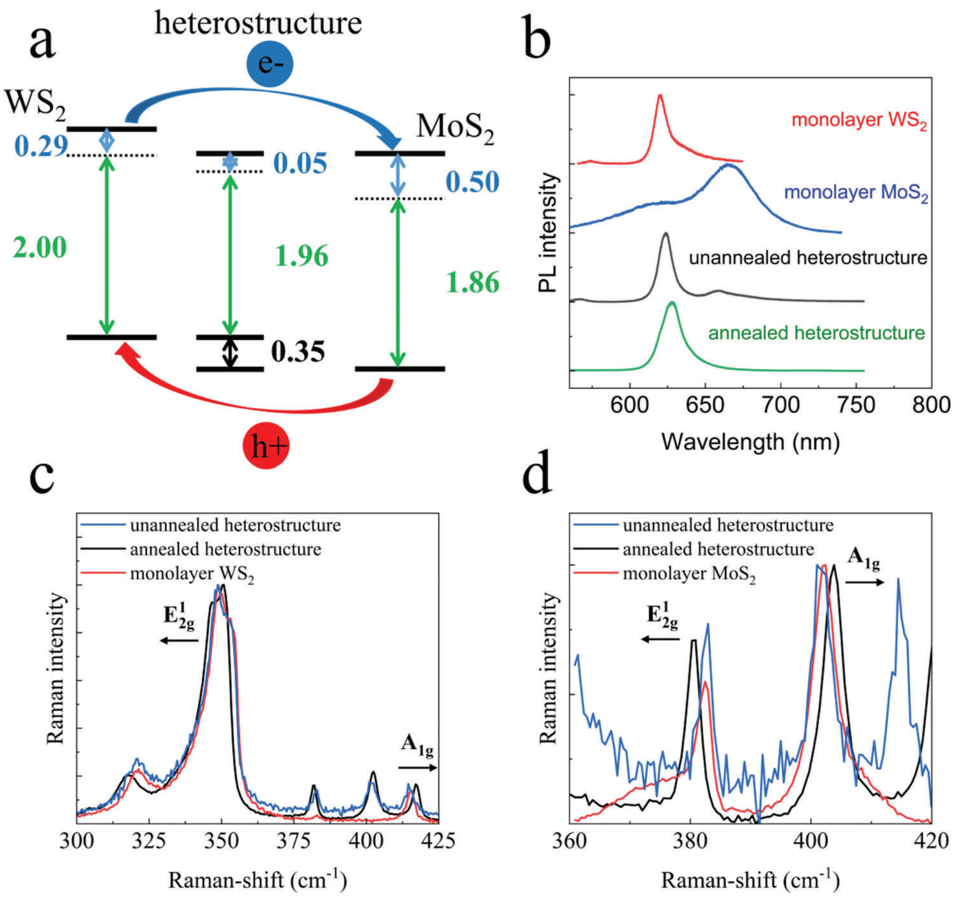

Figure 2. Interlayer transition. a) Schematic diagram of A exciton-coupled band alignment of WS_2/MoS_2 heterostructure. The solid black line represents the bottom of the conduction band and the top of valence band. PL spectra b) and Raman spectra c,d) of monolayer WS_2, MoS_2, unannealed and annealed WS_2/MoS_2 heterostructure. The arrows indicate the shift directions of Raman peaks. The substrate here is SiO_2/Si. WS_2 is on top of MoS_2 in our samples.

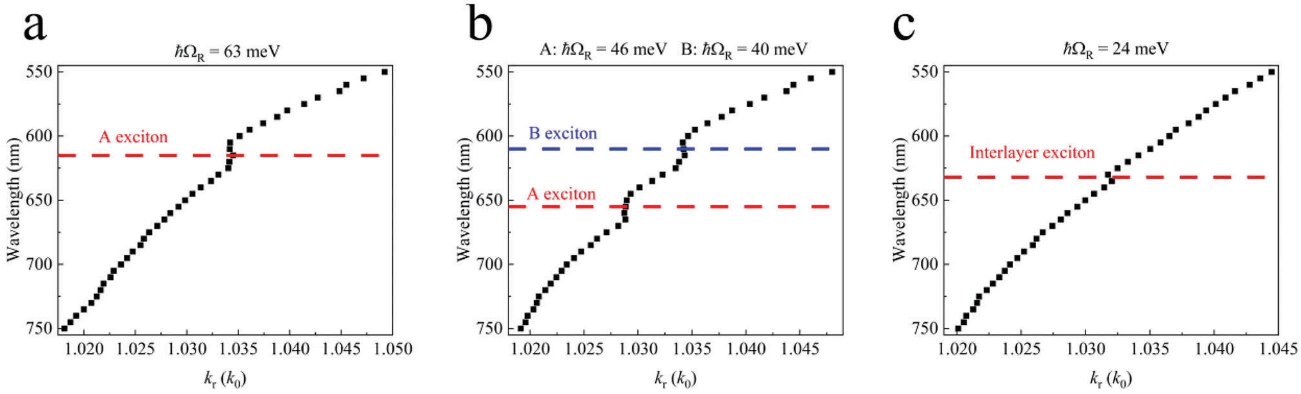

Figure 3. Measured dispersion relations of surface/interface exciton-plasmon polaritons. The 2D TMDCs are a) WS_2, b) MoS_2, and c) their heterostructure respectively. Red and blue dotted lines refer to positions of excitons.

The guided SPP wave mode can be generated at the air/Ag interface. After 2D material transfer, with excitons inside TMDCs, the interaction gives birth to a new hybrid mode, i.e., surface/interface exciton-plasmon polariton at the air/TMDC monolayer (heterostructure)/Ag interface, and Rabi oscillation phenomenon can occur.[42] **Figure 3** shows measured dispersion relations of surface/interface exciton-plasmon polaritons from WS_2, MoS_2 monolayers, and their heterostructure on single-crystalline Ag respectively. In the presence of A exciton and B exciton in MoS_2, two Rabi splitting positions can be seen, while for WS_2

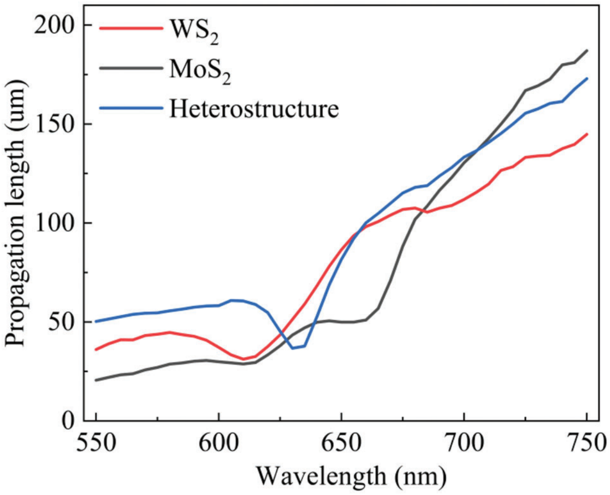

Figure 4. Propagation lengths were measured for surface/interface polaritons of structures with WS_2, MoS_2 monolayers, and their heterostructure on single-crystalline Ag respectively.

and WS_2/MoS_2 heterostructure, there is only one Rabi splitting position. The energy of Rabi splitting depends on the coupling strength. For WS_2 monolayer, due to its strong exciton resonance, the Rabi splitting energy can reach ≈63 meV. For MoS_2 monolayer, resonance strengths of excitons are weaker than that of WS_2, with Rabi splitting energies of 46 and 40 meV for A and B excitons respectively. The strength of the interlayer exciton in WS_2/MoS_2 heterostructure is comparatively weaker, such that the Rabi splitting energy produced by the interlayer exciton is only 24 meV.

Propagation length is another important property of surface/interface polariton waves. The propagation length of SPPs on the surface of single-crystalline Ag can be nearly 200 μm at wavelength of 700 nm (Figure S6, Supporting Information). It is much larger than the result from Johnson and Christy in 1972,[43] as well as that from Palik,[44] testifying to high-quality Ag crystals we synthesized. When 2D TMDCs are introduced on the Ag surface, the SPP wave turns into surface/interface exciton-plasmon polariton wave, as a result of coupling between the exciton in 2D TMDC and plasmon in Ag. This strong coupling significantly decreases the propagation length. **Figure 4** shows the measured propagation lengths of surface/interface exciton-plasmon polariton waves, where WS_2, MoS_2 monolayers, and their heterostructure are placed on single-crystalline Ag. Compared to that of SPP wave shown in Figure S6c, Supporting Information, the propagation lengths of surface/interface exciton-plasmon polariton waves drop down. At the very wavelength of exciton resonances, propagation length even drops to below 50 μm.

The complex dielectric function of as-grown single-crystalline Ag was first measured with the above procedure (Figure S6, Supporting Information), which is close but different to Johnson–Christy's data.[43] And then, the complex optical conductivities of WS_2 and MoS_2 monolayers were measured respectively. If 2D materials can be truly considered as a very thin layer, the optical conductivity ($\sigma_{2D} = \sigma_1 + i\sigma_2$) and dielectric function ($\varepsilon = \varepsilon_1 + i\varepsilon_2$) will be mutually converted by the following equation[45]

$$\sigma_{2D} = \sigma_{3D} d = -i\varepsilon_0 \omega (\varepsilon - 1) d \tag{3}$$

where d is the effective thickness of 2D materials. For comparison, we convert the dielectric functions of monolayer WS_2 and MoS_2 from some literature that have been reported[46,47] through the above equation and then put them together in **Figure 5** with our measured results. Figure 5a,b shows the real and imaginary parts of optical conductivity of WS_2 monolayer. In the visible range, there is mainly A exciton (≈615 nm), agreeing well with that in the PL spectrum shown in Figure S5a. Figure 5c,d shows the real and imaginary parts of optical conductivity of MoS_2 monolayer, in which A exciton (≈660 nm) and B exciton (≈620 nm) take place as those in the PL spectrum shown in Figure S5b, Supporting Information. From Equation (3), the real (imaginary) part of optical conductivity is related to the imaginary (real) part of the dielectric function. It can be seen that the real parts of optical conductivities for our WS_2 and MoS_2 monolayers are basically the smallest, as shown in Figure 5a,c, which is in accordance with their single-crystalline natures. On the other hand, the imaginary parts of optical conductivities relate to the strength of exciton resonance, thus those of our CVD-grown single-crystalline WS_2 and MoS_2 monolayers demonstrate the largest changes around exciton resonances, as shown in Figure 5b,d.

From a technical point of view, the measurement method we proposed above has a competitive advantage, i.e., the needed size of 2D materials can be much smaller than those of conventional optical methods. If the Fabry–Pérot cavity is replaced with that supporting whispering gallery mode to generate the interference fringes, the cavity could be shrunk, and the size requirement for the 2D material would be further reduced. Other comparisons are also briefly made between several measurement schemes (Table S1, Supporting Information). More importantly, from a physical point of view, the model we make use of is based on the surface polariton waves with surface/interface susceptibility, which facilitates the sensing of subtle change even at the level of a single layer of atoms. To that end, we measured optical conductivity of vertical heterostructures composed of single-crystalline WS_2 and MoS_2 monolayers. After the above interferometric measurements were performed, complex optical conductivity of WS_2/MoS_2 heterostructure was analyzed with the measured complex dielectric function of single-crystalline Ag, as shown in Figure 5f. Compared to those of WS_2 and MoS_2 monolayers, the resonant intensity of interlayer excitons (≈625 nm) of WS_2/MoS_2 heterostructure is weak. The change range of σ_2 at exciton resonance is ≈4.1×10^{-4} S for WS_2 monolayer (Figure 5b), 3.5×10^{-4} S for MoS_2 monolayer (Figure 5d) and 2.1×10^{-4} S for WS_2/MoS_2 heterostructure (Figure 5f), revealing that there is no change on the order of magnitude. Such a proportional relation is in agreement with that of Rabi splitting energies shown in Figure 3. In addition, the optical path of measurements is compatible with applied bias voltage, electric field, magnetic field, temperature, and other extrinsic variables, which enrich the properties and applications of 2D materials. Furthermore, our method is suitable for the measurements of anisotropic conductivities and other multilayer structures by modifying the underlying

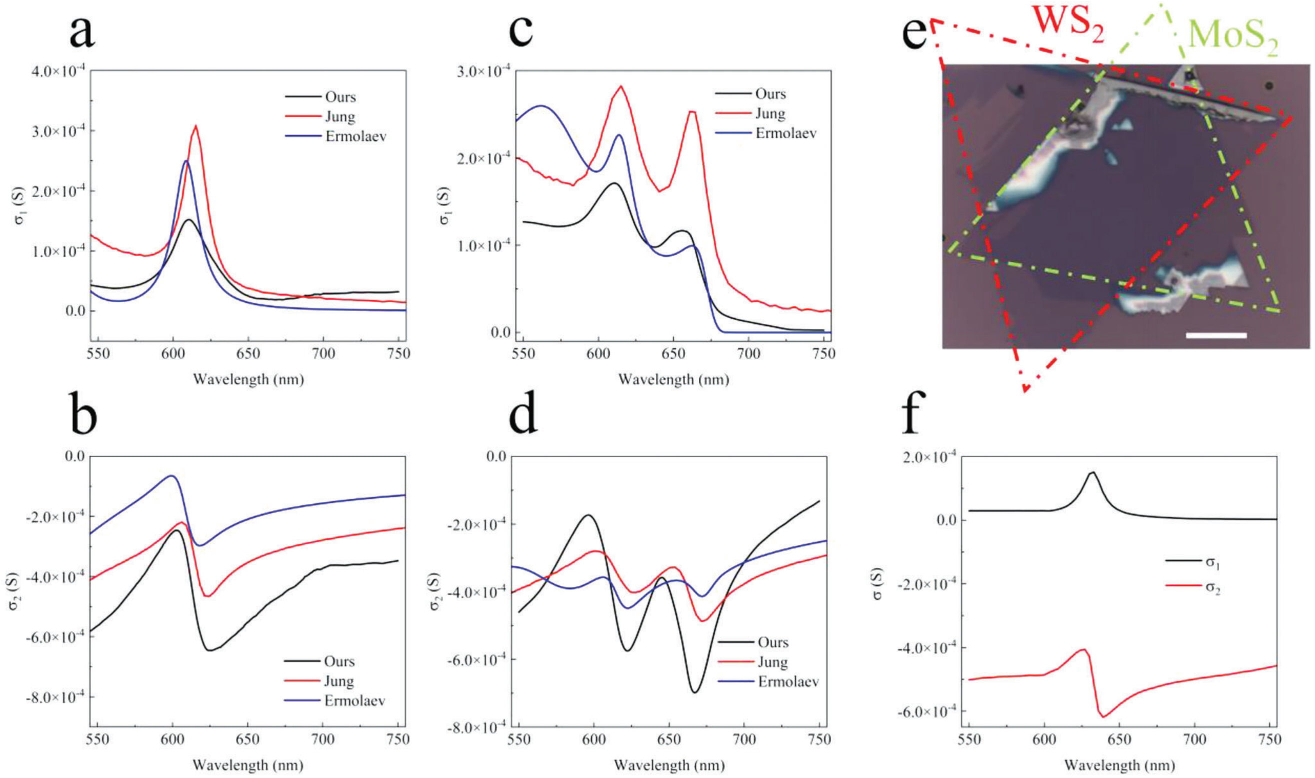

Figure 5. Measured optical conductivities. Real and imaginary parts of optical conductivity for a,b) WS_2 and c,d) MoS_2 monolayers. The thickness of MoS_2 and WS_2 monolayers is set as 0.65 nm.[18] e) Optical image of WS_2/MoS_2 heterostructure on SiO_2/Si substrate. Red and green triangles mark the contours of two elemental materials respectively. The scale bar is 25 µm. f) Measured optical conductivity of WS_2/MoS_2 heterostructure.

physical model, i.e., the dispersion relation of surface/interface polariton waves.

3. Conclusion

In conclusion, we have proposed a new method based on interference characteristics to measure complex optical conductivities of 2D materials. The high accuracy of the measurement is ensured by excitation and extraction of surface/interface polariton, a kind of evanescent wave. Single-crystalline Ag with low losses is utilized to support SPP and other surface/interface polariton waves with 2D materials at the interfaces, and promise significant interference phenomena of surface/interface polariton waves. By the interference of surface/interface exciton-plasmon polariton waves, the measurements of complex optical conductivity of WS_2 and MoS_2 TMDC monolayers with small crystal sizes are demonstrated. In terms of interlayer excitons, complex optical conductivity of WS_2/MoS_2 heterostructure is also measured via the interference effect of surface/interface interlayer exciton-plasmon polariton waves. Compared to traditional methods, the requirement imposed on material size in our measurements is much relieved, and the data extraction is convenient owing to simple physical model. Our method can be adopted to measuring anisotropic optical conductivities, other architectures of 2D materials, and the influence of ambient conditions.

4. Experimental Section

Single-Crystalline Ag Growth: The single-crystalline Ag was synthesized by a polyol reduction method catalyzed by platinum (Pt) nanoparticles and controlled by ammonium hydroxide (NH_3OH). The steps are as follows. 2.5 mmol silver nitrates ($AgNO_3$, HUSHI) and 15 ml ethylene glycol solution (EG, AR, HUSHI) as precursors were poured into a glass conical flask. Then 3 ml ammonium hydroxide (NH_3OH, 25%–28%, HUSHI) was added. Magnetic stirring was used to mix when 0.46 g polyvinylpyrrolidone ($M_w = 55\,000$, Sigma-Aldrich) was added. Afterward, 8 µl chloroplatinic acid (H_2PtCl_6, 8% in H_2O, Aladdin) was added, and 1.8 ml hydrogen peroxide (H_2O_2, 30%, HUSHI) was injected into the solution to reduce Ag. Later, single-crystalline Ag plates were synthesized after 5–7 days' reaction at room temperature. The Ag crystals were purged by deionized water, acetone, and ethyl alcohol, and preserved in alcohol.

2D Materials and Heterostructures Preparation: Experimentally, single-crystalline WS_2 and MoS_2 monolayers were synthesized by CVD growth. For MoS_2 monolayers, the MoO_3 powder doped with a small amount of NaCl was placed in the central zone of the furnace, and some sulfur powders were placed 18 cm away from it. The furnace was vacuumed and flushed with Ar gas for three times to exhaust the air. It heats up to 800 °C at a heating rate of 50 °C per minute and preserved for 3 min, then cools rapidly to room temperature. Under the protection of 80 sccm Ar gas, monolayers of MoS_2 can grow on the Si wafer with an oxide layer of 280 nm thickness. The furnace maintains one atmosphere of pressure throughout the process. For WS_2 monolayers, the growth temperature was changed to 850 °C and the WO_3 should be used. The WS_2/MoS_2 vertical heterostructures were obtained by dry transfer method. To improve the interlayer interaction, air molecules, and water molecules in the middle of the heterostructure need to be expelled with annealing of the heterostructure at 200 °C for 12 h in a 50 sccm Ar gas (containing 5% H_2) protection.

Supporting Information

Supporting Information is available from the Wiley Online Library or from the author.

Acknowledgements

This work was supported by the National Key Research and Development Program of China (2022YFA1405004, 2020YFA0211404, 2018YFA0306200, and 2017YFA0303700), the National Natural Science Foundation of China (11274159 and 11374150), and the Natural Science Foundation of Jiangsu Province, Major Project (BK20212004).

Conflict of Interest

The authors declare no conflict of interest.

Data Availability Statement

The data that support the findings of this study are available from the corresponding author upon reasonable request.

Keywords

2D materials, interlayer excitons, optical conductivity, surface exciton-plasmon polaritons, van der Waals heterostructures

Received: May 26, 2023
Revised: August 7, 2023
Published online: August 26, 2023

[1] K. S. Novoselov, A. K. Geim, S. V. Morozov, D. Jiang, Y. Zhang, S. V. Dubonos, I. V. Grigorieva, A. A. Firsov, *Science* **2004**, *306*, 666.
[2] K. F. Mak, M. Y. Sfeir, Y. Wu, C. H. Lui, J. A. Misewich, T. F. Heinz, *Phys. Rev. Lett.* **2008**, *101*, 196405.
[3] C. F. Chen, C. H. Park, B. W. Boudouris, J. Horng, B. Geng, C. Girit, A. Zettl, M. F. Crommie, R. A. Segalman, S. G. Louie, F. Wang, *Nature* **2011**, *471*, 617.
[4] M. Liu, X. Yin, E. Ulin-Avila, B. S. Geng, T. Zentgraf, L. Ju, F. Wang, X. Zhang, *Nature* **2011**, *474*, 64.
[5] W. Y. Wei, Y. P. Q. Yi, J. Song, X. G. Chen, J. H. Li, J. S. Li, *ACS Appl. Mater. Interfaces* **2022**, *14*, 13790.
[6] C. Ma, S. F. Yuan, P. Cheung, K. Watanabe, T. Taniguchi, F. Zhang, F. N. Xia, *Nature* **2022**, *604*, 266.
[7] T. Yu, F. Wang, T. Xu, L. Ma, X. Pi, D. Yang, *Adv. Mater.* **2016**, *28*, 4912.
[8] Q. Wang, K. K. Zadeh, A. Kis, J. N. Coleman, M. S. Strano, *Nat. Nanotechnol.* **2012**, *7*, 699.
[9] K. F. Mak, C. Lee, J. Hone, J. Shan, T. F. Heinz, *Phys. Rev. Lett.* **2010**, *105*, 136805.
[10] Y. Li, Y. Rao, K. F. Mak, Y. You, S. Wang, C. R. Dean, T. F. Heinz, *Nano Lett.* **2013**, *13*, 3329.
[11] Y. J. Gong, J. H. Lin, X. L. Wang, G. Shi, S. D. Lei, Z. Lin, X. L. Zou, G. L. Ye, R. Vajtai, B. I. Yakobson, H. Terrones, M. Terrones, B. K. Tay, J. Lou, S. T. Pantelides, Z. Liu, W. Zhou, P. M. Ajayan, *Nat. Mater.* **2014**, *13*, 1135.
[12] M. Baranowski, A. Surrente, L. Klopotowski, J. M. Urban, N. Zhang, D. K. Maude, K. Wiwatowski, S. Mackowski, Y. C. Kung, D. Dumcenco, A. Kis, P. Plochocka, *Nano Lett.* **2017**, *17*, 6360.
[13] P. Rivera, J. R. Schaibley, A. M. Jones, J. S. Ross, S. F. Wu, G. Aivazian, P. Klement, K. Seyler, G. Clark, N. J. Ghimire, J. Q. Yan, D. G. Mandrus, W. Yao, X. D. Xu, *Nat. Commun.* **2015**, *6*, 6242.
[14] A. M. Jones, H. Yu, N. J. Ghimire, S. Wu, G. Aivazian, J. S. Ross, B. Zhao, J. Yan, D. G. Mandrus, D. Xiao, W. Yao, X. Xu, *Nat. Nanotechnol.* **2013**, *8*, 634.
[15] A. M. Jones, H. Yu, J. R. Schaibley, J. Yan, D. G. Mandrus, T. Taniguchi, K. Watanabe, H. Dery, W. Yao, X. Xu, *Nat. Phys.* **2016**, *12*, 323.
[16] H. L. Liu, T. Yang, J. H. Chen, H. W. Chen, H. H. Guo, R. Saito, M. Y. Li, L. J. Li, *Sci. Rep.* **2020**, *10*, 15282.
[17] C. W. Hsu, R. Frisenda, R. Schmidt, A. Arora, S. M de Vasconcellos, R. Bratschitsch, H. S. J. van der Zant, A Castellanos-Gomez, *Adv. Opt. Mater.* **2019**, *7*, 1900239.
[18] B. K. Song, H. G. Gu, M. S. Fang, X. G. Chen, H. Jiang, R. Y. Wang, T. Y. Zhai, Y. T. Ho, S. Y. Liu, *Adv. Opt. Mater.* **2019**, *7*, 1801250.
[19] J. W. Park, H. S. So, S. Kim, S. H. Choi, H. Lee, J. Lee, C. Lee, Y. Kim, *J. Appl. Phys.* **2014**, *116*, 183509.
[20] M. I. Kazi, S. Ron, I. Timothy, O. Isaac, G. Nathan, D. E. Matthew, *Adv. Photonics Res.* **2021**, *2*, 2000180.
[21] G. A. Ermolaev, D. I. Yakubovsky, Y. V. Stebunov, A. V. Arsenin, V. S. Volkov, *J. Vac. Sci. Technol., B* **2020**, *38*, 014002.
[22] B. Munkhbat, P. Wróbel, T. J. Antosiewicz, T. O. Shegai, *ACS Photonics* **2022**, *9*, 2398.
[23] R. Kenaz, R. Rapaport, *Rev. Sci. Instrum.* **2023**, *94*, 023908.
[24] l. Asinovski, D. Beaglehole, M. T. Clarkson, *Phys. Status Solidi A* **2008**, *205*, 764.
[25] W. F. Shen, C. G. Hu, J. Tao, J. Liu, S. Q. Fan, Y. X. Wei, C. H. An, J. C. Chen, S. Wu, Y. N. Li, J. Liu, D. H. Zhang, L. D. Sun, X. T. Hu, *Nanoscale* **2018**, *10*, 8329.
[26] A. Ashoka, R. R. Tamming, A. V. Girija, H. Bretscher, S. D. Verma, S. D. Yang, C. H. Lu, J. M. Hodgkiss, D. Ritchie, C. Chen, C. G. Smith, C. Schnedermann, M. B. Price, K. Chen, A. Rao, *Nat. Commun.* **2022**, *13*, 1437.
[27] F. Hu, Y. Luan, J. Speltz, D. Zhong, C. H. Liu, J. Yan, D. G. Mandrus, X. Xu, Z. Fei, *Phys. Rev. B* **2019**, *100*, 121301.
[28] S. Zhang, B. C. Li, X. Z. Chen, F. L. Ruta, Y. M. Shao, A. J. Sternbach, A. S. McLeod, Z. Y. Sun, L. Xiong, S. L. Moore, X. Y. Xu, W. J. Wu, S. Shabani, L. Zhou, Z. Y. Wang, S. Mooshammer, E. Ray, N. Wilson, P. J. Schuck, C. R. Dean, A. N. Pasupathy, M. Lipson, X. D. Xu, X. Y. Zhu, A. J. Millis, M. K. Liu, J. C. Hone, D. N. Basov, *Nat. Commun.* **2022**, *13*, 542.
[29] M. Merano, *Phys. Rev. A* **2016**, *93*, 013832.
[30] G. Jayaswal, Z. Y. Dai, X. X. Zhang, M. Bagnarol, A. Martucci, M. Merano, *Opt. Lett.* **2018**, *43*, 703.
[31] C. Y. Wang, H. Y. Chen, L. Y. Sun, W. L. Chen, Y. M. Chang, H. Y. Ahn, X. Q. Li, S. Gwo, *Nat. Commun.* **2015**, *6*, 7734.
[32] H. Z. Liang, D. J. Kim, H. S. Chung, J. Zhang, K. N. Yu, S. H. Li, R. X. Li, *Acta Phys. -Chim. Sin.* **2003**, *19*, 150.
[33] P. A. D. Gonçalves, N. M. R. Peres, D. Wagner, U. Kreibig, M. Rogers, F. Hofer, F. R. Aussenegg, J. R. Krenn, *An Introduction to Graphene Plasmonics*, World Scientific, Singapore **2016**.
[34] H. Ditlbacher, A. Hohenau, D. Wagner, U. Kreibig, M. Rogers, F. Hofer, F. R. Aussenegg, J. R. Krenn, *Phys. Rev. Lett.* **2005**, *95*, 257403.
[35] S. Tongay, W. Fan, J. Kang, J. Park, U. Koldemir, J. Suh, D. S. Narang, K. Liu, J. Ji, J. B. Li, R. Sinclair, J. Q. Wu, *Nano Lett.* **2014**, *14*, 3185.
[36] A. Berkdemir, H. R. Gutiérrez, A. R. Botello-Méndez, N. Perea-López, A. L. Elías, C. I. Chia, B. Wang, V. H. Crespi, F. López-Urías, J. C Charlier, *Sci Rep* **2013**, *3*, 1755.
[37] W. J. Zhao, Z. Ghorannevis, K. K. Amara, J. R. Pang, M. L. Toh, X. Zhang, C. Kloc, P. H. Tan, G. Eda, *Nanoscale* **2013**, *5*, 9677.
[38] C. H. Lee, H. G. Yan, L. E. Brus, T. F. Heinz, J. Hone, S. Ryu, *ACS Nano* **2010**, *4*, 2695.
[39] X. Hong, J. Kim, S. F. Shi, Y. Zhang, C. Jin, Y. Sun, S. Tongay, J. Wu, Y. Zhang, F. Wang, *Nat. Nanotechnol.* **2014**, *9*, 682.

[40] K. Kośmider, J. Fernández-Rossier, *Phys. Rev. B* **2013**, *87*, 075451.

[41] K. F. Mak, K. He, C. Lee, G. H. Lee, J. Hone, T. F. Heinz, J. Shan, *Nat. Mater.* **2013**, *12*, 207.

[42] P. A. D. Gonçalves, L. P. Bertelsen, S. S. Xiao, N. A. Mortensen, *Phys. Rev. B* **2018**, *97*, 041402.

[43] P. B. Johnson, R. W. Christy, *Phys. Rev. B* **1972**, *6*, 12.

[44] E. D. Palik, *Handbook of Optical Constants of Solids*, Academic Press, Inc, United States of America **1985**.

[45] Y. L. Li, A. Chernikov, X. Zhang, A. Rigosi, H. M. Hill, A. M. van der Zande, D. A. Chenet, E. M. Shih, J. Hone, T. F. Heinz, *Phys. Rev. B* **2014**, *90*, 205422.

[46] G. H. Jung, S. Yoo, Q. H. Park, *Nanophotonics* **2019**, *8*, 263.

[47] G. A. Ermolaev, Y. V. Stebunov, A. A. Vyshnevyy, D. E. Tatarkin, D. I. Yakubovsky, S. M. Novikov, D. G. Baranov, T. Shegai, A. Y. Nikitin, A. V. Arsenin, V. S. Volkov, *npj 2D Mater. Appl.* **2020**, *4*, 21.